Single-electron quantum tomography in quantum Hall edge channels

New Journal of Physics

Single-electron quantum tomography in quantum Hall edge channels

Ch Grenier[1]**, R Hervé**[2]**, E Bocquillon**[2]**, F D Parmentier**[2]**,
B Plaçais**[2]**, J M Berroir**[2]**, G Fève**[2] **and P Degiovanni**[1,3]

[1] Université de Lyon, Fédération de Physique André Marie Ampère,
CNRS-Laboratoire de Physique de l'Ecole Normale Supérieure de Lyon,
46 Allée d'Italie, 69364 Lyon Cedex 07, France
[2] Laboratoire Pierre Aigrain, Département de Physique de l'Ecole Normale
Supérieure, 24 rue Lhomond, 75231 Paris Cedex 05, France
E-mail: Pascal.Degiovanni@ens-lyon.fr

Abstract. We propose a quantum tomography protocol to measure single-electron coherence in quantum Hall edge channels, and therefore access for the first time the wavefunction of single-electron excitations propagating in ballistic quantum conductors. Its implementation would open the way to quantitative studies of single-electron decoherence and would provide a quantitative tool for analyzing single- to few-electron sources. We show how this protocol could be implemented using ultrahigh-sensitivity noise measurement schemes.

[3] Author to whom any correspondence should be addressed.

IOP Institute of Physics Φ DEUTSCHE PHYSIKALISCHE GESELLSCHAFT

Contents

1. Introduction

Electron quantum optics aims at controlled manipulation and measurement of the quantum state of a single to a few electrons propagating in the solid state, in a comparable way to recent achievements with microwave photons [1, 2] or light [3]. In particular, it requires the use of ballistic quantum conductors where single electrons can propagate along one-dimensional (1D) modes. Using continuous sources, Mach–Zehnder interferometers have been realized in integer quantum Hall edge channels, demonstrating single-electron [4–6] as well as two-electron [7] quantum coherence following a proposal by Samuelsson *et al* [8]. Recently, an on-demand single-electron and single-hole source based on the mesoscopic capacitor was demonstrated [9, 10]. A two-terminal single-electron and single-hole source based on a dynamical quantum dot [11] operating at GHz frequencies has also been demonstrated in a quantum Hall edge channel, as well as a similar electron pump in a 2D electron gas (2DEG) at zero magnetic field [12]. Single-electron excitations can also be generated at GHz repetition rates using surface acoustic waves [13, 14] and can be detected with high efficiency after propagation within a 1D non-chiral channel [15]. All these developments in quantum transport and single-electron electronics have given hopes of realizing electron quantum optics experiments involving single-electron excitations [16, 17].

In this context, it is important to understand precisely the similitudes and differences between electron quantum optics and photonic quantum optics. The Fermi statistics of electrons is expected to bring in new features. First of all, the ground state of a metallic conductor is a Fermi sea characterized by its chemical potential. Fermi sea vacua have radically different properties from the photon vacuum since, due to Fermi statistics, entanglement can be generated by sources at equilibrium even in the absence of interactions [18]. In addition to quantum statistics, Coulomb interactions lead to decoherence of electronic excitations whose

consequences in the context of Mach–Zehnder interferometers have been extensively discussed in recent years [19–25].

However, with the advent of on-demand single-electron sources, the problem of electronic decoherence has to be reconsidered. A crucial question is to understand the deviation from the non-interacting picture for single-electron excitations emitted by these new sources due to electron–electron interactions and to decoherence induced by the electromagnetic environment. As suggested by recent experimental studies of electron relaxation in quantum Hall edge channels [26, 27], these effects seriously question the quantum optics paradigm of electronic quasiparticles in quantum Hall edge channels. Although this problem has been investigated on the theoretical side [28], it is important to develop new experimental tools that allow us to tackle these issues in a direct and accessible way.

For this reason, we propose a quantum tomography protocol for single-electron excitations in quantum Hall edge channels in the spirit of homodyne tomography in quantum optics [29, 30]. Despite the recent experimental achievements in electron quantum optics, the quantum state of a single-electron excitation has never been imaged and our proposal is designed to fill this gap. Performing such single-electron quantum tomography would then open the way to experimental studies of single-electron decoherence in nanostructures and consequently to quantitative tests of theoretical approaches to this basic problem [28]. Our single-electron quantum tomography protocol would also lead to a new characterization of the quantum coherence properties of single- to few-electron sources [9, 11, 31].

To support its feasibility, we discuss predictions for the experimental signals produced by a realistic source of energy-resolved single-electron excitations emitted by the mesoscopic capacitor [9]. Our study shows that this proposal could be implemented using recently developed ultrahigh-sensitivity noise measurement schemes [32]. We also discuss quality assessment for the coherence of single-electron sources in terms of quantum information concepts such as linear entropy and fidelity with respect to trial single-electron wavefunctions. We show how these quantities can be accessed through full quantum tomography of single-electron excitations.

This paper is structured as follows: the notion of single-electron coherence is recalled and briefly discussed in section 2. Our proposal for a single-electron quantum tomography protocol is then described in section 3. Finally, predictions and quality assessment for the on-demand single-electron source are presented in section 4.

2. Single-electron coherence

For a many-body system, the quantum coherence properties at the single-particle level are encoded within the space and time dependence of the two-point Green's function, called the single-electron coherence, and analogous to field correlations introduced by Glauber [33] for photons:

$$\mathcal{G}^{(e)}(x, t; x', t') = \langle \psi^\dagger(x', t') \psi(x, t) \rangle, \tag{1}$$

where operators $\psi(x)$ and $\psi^\dagger(x)$ destroy and create a single electron at position x. In the same way, the single-hole coherence is defined as

$$\mathcal{G}^{(h)}(x, t; x', t') = \langle \psi(x', t') \psi^\dagger(x, t) \rangle. \tag{2}$$

In this paper, we consider ballistic conductors formed by a single quantum edge Hall channel. Thus, electron propagation within the edge channel is chiral at the Fermi velocity v_F so that

the single-electron coherence obeys this property. Since measurements are usually made at a given position, we will focus on the time dependence at a given position, which by chirality also characterizes spatial coherence properties.

In full generality, the single-electron coherence can be decomposed as the sum of an equilibrium contribution $\mathcal{G}_{\mu}^{(e)}$ due to the Fermi sea $|F_{\mu}\rangle$ at the electrochemical potential μ and an extra contribution $\Delta\mathcal{G}^{(e)}(t, t')$ representing single-particle coherence of excitations emitted by sources within the conductor:

$$\mathcal{G}^{(e)}(t, t') = \mathcal{G}_{\mu}^{(e)}(t - t') + \Delta\mathcal{G}^{(e)}(t, t'). \tag{3}$$

Note that any stationary single-particle coherence such as $\mathcal{G}_{\mu}^{(e)}$ only depends on $t - t'$ and not on $\bar{t} = (t + t')/2$. Since we are interested in single-electron sources that produce a non-stationary single-electron coherence, the $\bar{t}$ dependence of $\Delta\mathcal{G}^{(e)}(t, t')$ must be retained. Note that $-ev_{\mathrm{F}}\Delta\mathcal{G}^{(e)}(t, t)$ is the average excess current measured at position x and time t.

As an example, let us consider an ideal one-shot single-electron source that would inject an electronic excitation in wavepacket φ_{e} above the Fermi sea, i.e. such that in the frequency domain $\varphi_{\mathrm{e}}(\omega) = 0$ for $\omega \leqslant 0$. This ideal source would generate the many-body state

$$\psi^{\dagger}[\varphi_{\mathrm{e}}]|F_{\mu}\rangle = \int \varphi_{\mathrm{e}}(x)\psi^{\dagger}(x)|F_{\mu}\rangle\,\mathrm{d}x. \tag{4}$$

Then, using Wick's theorem, the single-electron coherence at $x = 0$ due to the single excitation can be readily evaluated:

$$\Delta\mathcal{G}_{\psi^{\dagger}[\varphi_{\mathrm{e}}]|F_{\mu}\rangle}^{(e)}(t, t') = \varphi_{\mathrm{e}}(-v_{\mathrm{F}}t)\,\varphi_{\mathrm{e}}^{*}(-v_{\mathrm{F}}t'). \tag{5}$$

This example shows that an experimental determination of $\Delta\mathcal{G}^{(e)}$ provides a direct visualization of wavefunctions of coherent single-electron excitations. However, in any real device, many-particle correlations due to the Pauli exclusion principle [34] and Coulomb interactions may lead to relaxation and decoherence of single-electron or single-hole excitations [28]. Then, because of decoherence, $\Delta\mathcal{G}^{(e)}(t, t')$ is not of the simple form given by (5). Nevertheless, its behavior in $|t - t'|$ still describes the temporal coherence of the electrons at the position of measurement and thus provides information on their coherence time. Accessing the coherence properties of energy-resolved single-electron excitations is crucial for probing the chiral Fermi liquid paradigm in quantum Hall edge channels in the spirit of Landau's original discussion of the quasiparticle concept [35].

In practice, since sub-nanosecond detection of a single electron cannot be achieved in the present status of technology, it is more convenient to access the coherence of single-particle excitations in the frequency domain:

$$\Delta\mathcal{G}^{(e)}(t, t') = \int \Delta\mathcal{G}^{(e)}(\omega_{+}, \omega_{-})\,\mathrm{e}^{\mathrm{i}(\omega_{-}t' - \omega_{+}t)}\,\frac{\mathrm{d}\omega_{+}\,\mathrm{d}\omega_{-}}{(2\pi)^{2}}, \tag{6}$$

where ω_{+} and ω_{-} are, respectively, conjugated to t and t'. In the frequency domain, the stationary part is encoded within the diagonal $\omega_{+} = \omega_{-}$, whereas the non-stationarity of single-electron coherence is encoded in its $\Omega = \omega_{+} - \omega_{-}$ dependence. Let us remember that electron distribution function measurements [26] only give access to the stationary part of the single-electron coherence (diagonal $\omega_{+} = \omega_{-}$ or equivalently $\Omega = 0$), but fail to capture its $\bar{t} = (t + t')/2$ dependence encoded in the off-diagonal terms of the single-electron coherence in frequency space: $\mathcal{G}^{(e)}(\omega_{+}, \omega_{-})$ for $\omega_{+} \neq \omega_{-}$.
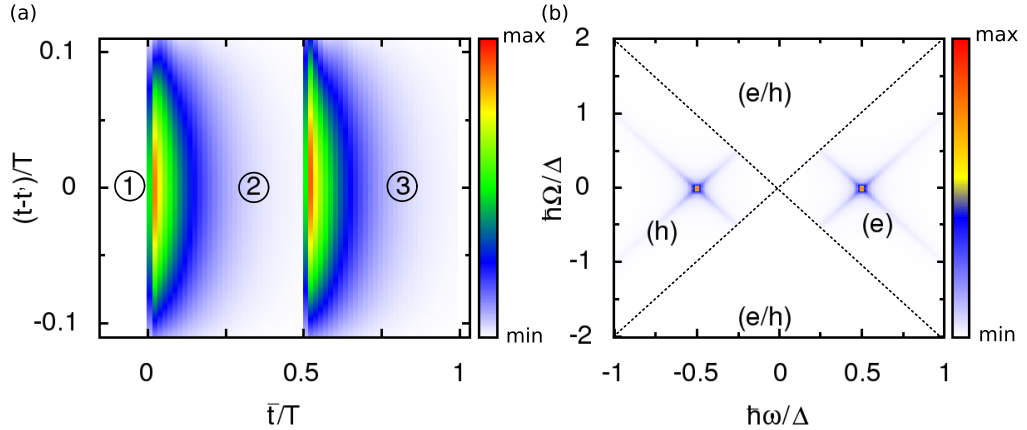
Figure 1. Expected single-electron coherence from the single-electron source [9] at the electron hole symmetric point: $\hbar\omega_e = -\hbar\omega_h = \Delta/2$: (a) $|v_F \Delta \mathcal{G}^{(e)}(t, t')|$ from the discrete level coupled to a continuum approach ($h\gamma_e/\Delta \simeq 0.21$ and $T\gamma_e \simeq 6.85$). (b) Modulus of $\Delta\mathcal{G}^{(e)}$ in Fourier space: ω is conjugated to $t - t'$ and Ω to $\bar{t} = (t + t')/2$. Quadrants (e) (respectively (h)) represent electron (respectively hole) coherence, whereas the (e/h) quadrants encode electron/hole coherence. Energy-resolved single-electron (respectively hole) excitations can be seen in the (e) (respectively (h)) quadrants. The horizontal line $\Omega = 0$ gives the average excess electron occupation number due to the source.

Figure 1 presents density plots of single-electron coherence that would be emitted by an ideal on-demand single-electron source [9] based on the mesoscopic capacitor depicted in figure 2(a). Ideally, such a source should emit a single electron followed by a single-hole excitation: at $t = 0$, the highest occupied energy level of a quantum dot (see figure 2(b)) is moved at energy $\hbar\omega_e > 0$ above the Fermi level (taken for simplicity at zero) and releases a single electron in the continuum of available single-particle states $\varphi_\omega(x) = e^{i\omega x/v_F}$ ($\omega > 0$). The resulting single-particle wavefunction is obtained as a truncated Lorentzian in the frequency domain:

$$\widetilde{\varphi}_e(\omega) = \frac{\mathcal{N}_e \, \theta(\omega)}{\omega - \omega_e - i\gamma_e/2}, \tag{7}$$

where $\mathcal{N}_e$ ensures normalization and γ_e denotes the electron escape rate from the quantum dot. Hole emission starts at $t = T/2$ when electron emission is completed ($\gamma_e T \gg 1$) and is described in a similar way to the release of a single-hole truncated Lorentzian wavepacket at energy $\hbar\omega_h < 0$ in the continuum of available hole states below the Fermi level. Ideally, the source is expected to release a single electron and a single hole and therefore to generate the state $\psi^\dagger[\varphi_e]\psi[\varphi_h]|F_\mu\rangle$. Figure 1(a) presents a density plot for $|v_F \Delta\mathcal{G}^{(e)}(t, t')|$ for such a state as a function of $\bar{t} = (t + t')/2$ and $t - t'$: the electron and hole wavepackets emitted during each half-period are clearly seen. The $\bar{t}$ dependence for $t = t'$ is the exponential decay of the average electrical current as observed and characterized experimentally [36] and the decay of $|v_F \Delta\mathcal{G}^{(e)}(t, t')|$ along $|t - t'|$ reflects the truncation of the Lorentzian.

Figure 1(b) then presents a density plot of $|v_F \Delta\mathcal{G}^{(e)}(\omega_+, \omega_-)|$ as a function of $\omega = (\omega_+ + \omega_-)/2$ and $\Omega = \omega_+ - \omega_-$. Note that the quadrant (e) in figure 1(b), defined by both ω_+ and ω_- positive, corresponds to single-particle states with energy above the Fermi energy (electron
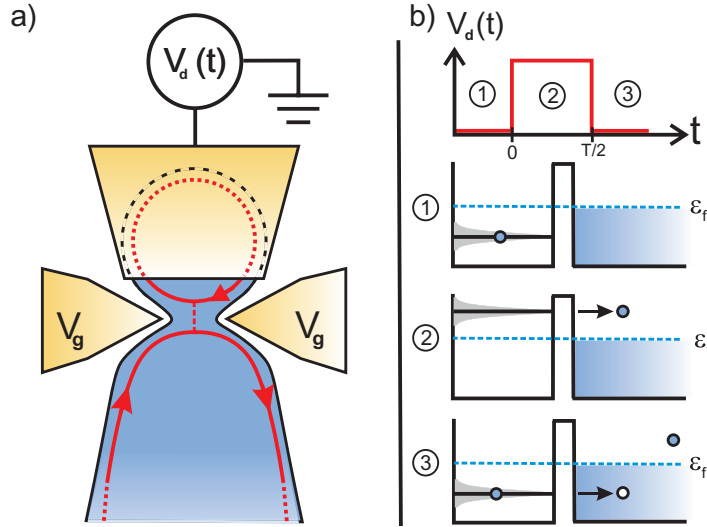
Figure 2. (a) A micron-sized dot with level spacing Δ and a tunable quantum point contact (QPC) is capacitively coupled to a top metallic gate. (b) Applying a square voltage $V_d(t)$ to the top gate brings a populated dot level above the Fermi level, thus emitting a single electron at energy $\hbar\omega_e = +\Delta/2$, followed by a single hole when the level is brought back at energy $\omega_h = -\Delta/2$ below the Fermi energy. The widths of these excitations $\gamma_{e,h}$ are given by the corresponding escape rates from the dot.

states). Similarly, the quadrant (h) with both ω_+ and ω_- negative corresponds to hole states. Figure 1(b) clearly exhibits energy-resolved electron and hole excitations.

The off-diagonal quadrants (e/h) in figure 1(b) are defined by $\omega_+\omega_- < 0$ and correspond to electron/hole coherence. Such an electron/hole coherence appears in superpositions of states with different electron/hole pair numbers such as, for example, $\alpha|F_\mu\rangle + \beta\psi^\dagger[\varphi_e]\psi[\varphi_h]|F_\mu\rangle$. In such a state, the single-electron coherence contains interference contributions of the form $\langle F_\mu|\psi^\dagger(x,t')\psi(x,t)\psi[\varphi_h]\psi^\dagger[\varphi_e]|F_\mu\rangle$ and $\langle F_\mu|\psi[\varphi_e]\psi^\dagger[\varphi_h]\psi^\dagger(x,t')\psi(x,t)|F_\mu\rangle$. Using Wick's theorem and assuming as before that $\varphi_{e/h}$ are, respectively, pure electron and hole wavefunctions, we obtain for example that $\langle F_\mu|\psi^\dagger(x,t')\psi(x,t)\psi[\varphi_h]\psi^\dagger[\varphi_e]|F_\mu\rangle = -\varphi_h(x - v_F t') * \varphi_e(x - v_F t)$. This shows that these interference contributions live in the (e/h) quadrants of the frequency domain. Let us point out again that an ideal single-electron and single-hole source should not exhibit electron/hole coherences.

3. Single-electron quantum tomography

To date, in mesoscopic conductors, a quantum tomography protocol has only been proposed for orbital states [37], but not for the reconstruction of temporal or spatial single-particle coherence. To achieve this goal, we propose the use of a Hanbury Brown and Twiss (HBT) setup [38–41] as depicted in figure 3(a). Our proposal is based on the analogy to optical tomography [29, 30], and its simple design, also proposed to realize a Hong–Ou–Mandel experiment [42] with single electrons [16], makes it a potentially general tool for electronic quantum coherence measurement.
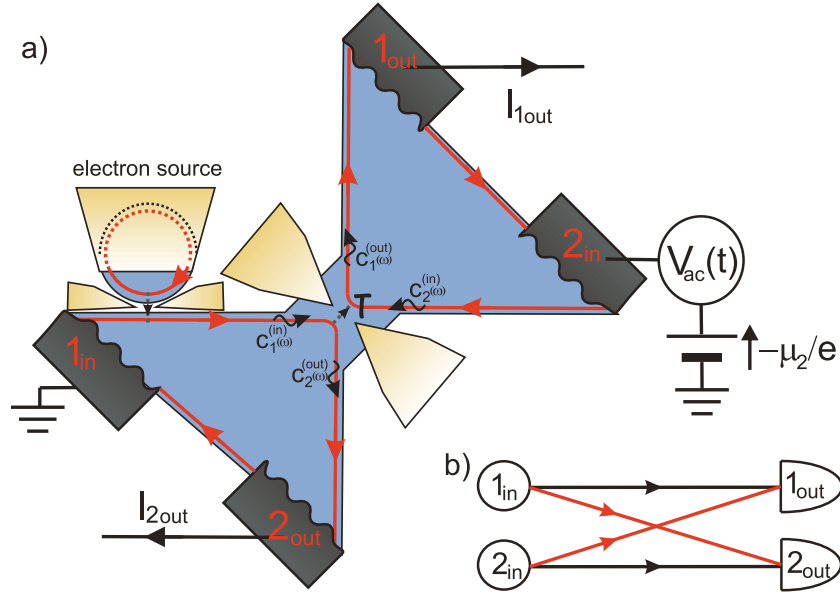
Figure 3. (a) The beam splitter is a QPC of transparency $\mathcal{T}$. The source is placed on incoming channel 1, whereas channel 2 at chemical potential μ_2 can be driven by $V_{ac}(t) = V\cos(2\pi n f t + \phi)$, where $f = 1/T$ is the driving frequency of the source. Outcoming current correlations are measured at low frequency. (b) The direct and exchange two-particle paths responsible for the HBT effect.

3.1. The Hanbury Brown and Twiss effect

The HBT effect arises from two-particle interferences between direct and exchange paths as depicted schematically in figure 3(b). These interferences lead to the bunching of indistinguishable bosons and the antibunching of indistinguishable fermions expected from their quantum statistics. As a consequence, when indistinguishable particles from two independent sources collide on a beam splitter, the outcoming particle current fluctuations and correlations encode information on the single-particle contents in the two incoming beams. Since its discovery [38, 43], the HBT effect has also been observed for electrons in a 2DEG issued by two different reservoirs at equilibrium [39–41]. Here, we discuss how the HBT effect manifests itself in outcoming current correlations in the HBT setup depicted in figure 3(a).

In this HBT setup, the quantum point contact (QPC) acts as a perfect electron beam splitter with energy-independent reflection and transmission probabilities $\mathcal{R}$ and $\mathcal{T}$ ($\mathcal{R} + \mathcal{T} = 1$). Let us introduce the incoming and outcoming electron modes within each channel ($\alpha \in \{1, 2\}$) as depicted in figure 3(a):

$$\psi_\alpha^{(in)}(t) = \int c_\alpha^{(in)}(\omega)\, e^{-i\omega t}\, \frac{d\omega}{\sqrt{2\pi v_F}}, \tag{8}$$

$$\psi_\alpha^{(out)}(t) = \int c_\alpha^{(out)}(\omega)\, e^{-i\omega t}\, \frac{d\omega}{\sqrt{2\pi v_F}}, \tag{9}$$

where $\psi_\alpha^{(in)}(t)$ denotes the electron field in channel α right before the QPC, whereas the $\psi_\alpha^{(out)}(t)$ are taken right after the QPC. The outcoming electron modes are then related to the incoming

ones by the QPC scattering matrix, which we take to be of the form

$$
\begin{pmatrix} c_1^{(\text{out})}(\omega) \\ c_2^{(\text{out})}(\omega) \end{pmatrix} = \begin{pmatrix} \sqrt{\mathcal{T}} & i\sqrt{\mathcal{R}} \\ i\sqrt{\mathcal{R}} & \sqrt{\mathcal{T}} \end{pmatrix} \begin{pmatrix} c_1^{(\text{in})}(\omega) \\ c_2^{(\text{in})}(\omega) \end{pmatrix}.
\tag{10}
$$

Using this scattering matrix, the outcoming current operators can be expressed in terms of the incoming fermion fields. Therefore, the outcoming current correlations defined as $S_{\alpha,\beta}^{\text{out}}(t,t') = \langle i_\alpha^{\text{out}}(t)\, i_\beta^{\text{out}}(t')\rangle - \langle i_\alpha^{\text{out}}(t)\rangle\langle i_\beta^{\text{out}}(t')\rangle$ $((\alpha,\beta)\in\{1,2\})$ can be computed in terms of incoming current and electronic correlations:

$$
S_{11}^{\text{out}}(t,t') = \mathcal{R}^2 S_{11}^{\text{in}}(t,t') + \mathcal{T}^2 S_{22}^{\text{in}}(t,t') + \mathcal{RT}\, \mathcal{Q}(t,t'),
\tag{11}
$$

$$
S_{22}^{\text{out}}(t,t') = \mathcal{T}^2 S_{11}^{\text{in}}(t,t') + \mathcal{R}^2 S_{22}^{\text{in}}(t,t') + \mathcal{RT}\, \mathcal{Q}(t,t'),
\tag{12}
$$

$$
S_{12}^{\text{out}}(t,t') = S_{21}^{\text{out}}(t,t') = \mathcal{RT}\left(S_{11}^{\text{in}}(t,t') + S_{22}^{\text{in}}(t,t') - \mathcal{Q}(t,t')\right),
\tag{13}
$$

where $S_{11}^{\text{in}}(t,t')$ and $S_{22}^{\text{in}}(t,t')$ denote the incoming current noises and $\mathcal{Q}(t,t')$ is the HBT contribution to outcoming correlations. Encoding two-particle interferences, it involves incoming single-electron and single-hole coherences at different times, right before the QPC:

$$
\mathcal{Q}(t,t') = (ev_{\text{F}})^2(\mathcal{G}_1^{(\text{e})}(t',t)\mathcal{G}_2^{(\text{h})}(t',t) + \mathcal{G}_2^{(\text{e})}(t',t)\mathcal{G}_1^{(\text{h})}(t',t)).
\tag{14}
$$

Equations (11)–(14) suggest that putting a suitable source on channel 2 of the HBT setup depicted in figure 3(a) would lead to the determination of single-electron coherence in channel 1 from current correlation measurements.

3.2. Quantum tomography: noise signals from single-electron coherence

In quantum optics, this idea has led to the homodyne quantum tomography of the state of a single quantum electromagnetic mode: in this case, channel 2 is fed with a coherent monochromatic radiation called the local oscillator, whose phase is used as a control parameter [29]. By analogy, in the present situation, the Ohmic contact on channel 2 will be used as a local oscillator since its chemical potential μ_2 can be varied to scan the relevant energy range of single-electron and single-hole excitations propagating along channel 1.

Contrary to the case of quantum optics experiments in the optical domain where the time-resolved arrival of single photons can be observed, counting single electrons on sub-nanosecond time scales cannot be achieved today. Our protocol will instead be based on the zero-frequency component of the average over $\bar{t}$ of current correlations

$$
S_{\alpha\beta}^{\text{exp}} = 2\int \overline{S_{\alpha,\beta}^{\text{out}}(\bar{t}+\tau/2,\bar{t}-\tau/2)}^{\bar{t}}\, d\tau,
\tag{15}
$$

which are standard experimentally accessible quantities in quantum transport experiments. Equations (11)–(13) show that these quantities now depend on the $\bar{t}$-average of the zero-frequency component of the HBT contribution $\mathcal{Q}(t,t')$:

$$
\mathcal{Q}_0(\omega=0) = \int \overline{\mathcal{Q}(\bar{t}+\tau/2,\bar{t}-\tau/2)}^{\bar{t}}\, d\tau.
\tag{16}
$$

Equation (14) shows that $\mathcal{Q}_0$ is nothing but the overlap between the single-electron and single-hole coherences of channels 1 and 2. The idea behind our tomography protocol is to find a suitable local oscillator to be able to reconstruct $\mathcal{G}_1^{(\text{e})}$ from measurements of this overlap.

Let us remark that $\mathcal{Q}_0(\omega = 0)$ contains contributions associated with the two input ohmic contacts that do not depend on the source's contribution to single-electron coherence $\Delta\mathcal{G}_1^{(e)}$. Those are present even when the source is turned off and thus are not relevant for reconstructing $\Delta\mathcal{G}_1^{(e)}$. The first one, given by $\mathcal{G}_{\mu_1}^{(e)}\mathcal{G}_{\mu_2}^{(h)} + \mathcal{G}_{\mu_1}^{(h)}\mathcal{G}_{\mu_2}^{(e)}$, contributes to the partition noise $S_{1,\mathrm{part}}^{\mathrm{exp}}(\mu_{12})$ associated with the dc bias $\mu_{12} = \mu_1 - \mu_2$ of the QPC [44, 45]. The second one, given by $\mathcal{G}_{\mu_1}^{(e)}\Delta\mathcal{G}_{\mu_2}^{(h)} + \mathcal{G}_{\mu_1}^{(h)}\Delta\mathcal{G}_{\mu_2}^{(e)}$, contributes to the photo-assisted noise $S_{1,\mathrm{pan}}^{\mathrm{exp}}[V_{\mathrm{ac}}(t)]$ due to the ac drive $V_{\mathrm{ac}}(t)$ theoretically predicted in [46–48] and experimentally studied in [49, 50]. Because the single-electron source generates no noise at zero frequency [10], the outcoming current noise in channel 1 can then be expressed in terms of the partition noise, the photo-assisted noise and the excess HBT contribution we are looking for:

$$S_{11}^{\mathrm{exp}} = S_{11,\mathrm{part}}^{\mathrm{exp}}(\mu_{12}) + S_{11,\mathrm{pan}}^{\mathrm{exp}}[V_{\mathrm{ac}}(t)] + \mathcal{RT}\Delta\mathcal{Q}_0[\omega = 0, \mu_2, V_{\mathrm{ac}}(t)], \tag{17}$$

where $\Delta\mathcal{Q}_0[\omega = 0, \mu_2, V_{\mathrm{ac}}(t)]$ denotes the excess HBT contribution which depends on the source's contribution $\Delta\mathcal{G}_1^{(e)}$. Thus, measuring the excess outcoming noise due to the source in one of the two channels directly gives access to the excess HBT contribution, which constitutes our experimental signal. As we shall see now, it contains all the information needed to reconstruct the single-electron coherence $\Delta\mathcal{G}_1^{(e)}$ emitted by the source.

In the experimentally relevant case of a T periodic source, $\Delta\mathcal{G}_1^{(e)}$ can be written as a Fourier transform with respect to $\tau = t - t'$ and a Fourier series with respect to $\bar{t} = (t + t')/2$. Therefore, single-electron tomography aims at reconstructing the harmonics $\Delta\mathcal{G}_{1,n}^{(e)}$ defined by

$$\Delta\mathcal{G}_1^{(e)}(t, t') = \sum_{n=-\infty}^{+\infty} e^{-2\pi i n\bar{t}/T} \int \Delta\mathcal{G}_{1,n}^{(e)}(\omega) e^{-i\omega\tau} \frac{\mathrm{d}\omega}{2\pi}. \tag{18}$$

Let us first discuss the $n = 0$ harmonic $v_{\mathrm{F}}\Delta\mathcal{G}_{1,n=0}^{(e)}(\omega)$, which represents the average density of electron excitations at energy $\hbar\omega$ emitted per period (the $\Omega = 0$ line in figure 1(b)). As this quantity is an average over $\bar{t}$, no homodyning is required and thus no ac voltage is applied: $V_{\mathrm{ac}}(t) = 0$. At zero temperature, the variation of the experimental signal $\Delta\mathcal{Q}_0$ with μ_2 reflects the single-particle content of the source at the corresponding energy:

$$\frac{\partial(\Delta\mathcal{Q}_0)}{\partial\mu_2}[\omega = 0, \mu_2, V_{\mathrm{ac}}(t) = 0] = -\frac{2e^2}{h} v_{\mathrm{F}}\Delta\mathcal{G}_{1,n=0}^{(e)}(\mu_2/\hbar). \tag{19}$$

Indeed, if the potential μ_2 becomes comparable to the energy of the emitted single-electron state, the latter will always find an indistinguishable partner in the second incoming channel of the beam splitter so that the excess partition noise due to the source vanishes. This is reflected by the minus sign in the rhs of equation (19). Finally, by varying the potential μ_2, one can measure the energy distribution of single-electron excitations in channel 1.

Let us now consider the higher harmonics $\Delta\mathcal{G}_{1,n}^{(e)}(\omega)$ with $n \neq 0$ which contain the $\bar{t}$ dependence of the single-electron coherence. Accessing $\Delta\mathcal{G}_{1,n}^{(e)}(\omega)$ requires homodyning the $\bar{t}$ dependence of $\Delta\mathcal{G}_1^{(e)}(t, t')$ at frequency nf ($f = 1/T$). This is achieved by applying an ac drive $V_{\mathrm{ac}}(t) = V\cos(2\pi nft + \phi)$ to the Ohmic contact on channel 2. At zero temperature, the linear response $\bar{\chi}_n(\mu_2, \phi) = [\partial(\Delta\mathcal{Q}_0)/\partial(eV/nhf)]|_{\omega=0, V=0}$ to the ac drive of the excess HBT contribution of the source is related to the single-electron coherence by

$$\frac{\partial\bar{\chi}_n}{\partial\mu_2}(\mu_2, \phi) = \frac{e^2}{h}\Re\left[e^{i\phi}\left(v_{\mathrm{F}}\Delta\mathcal{G}_{1,n}^{(e)}\left(\frac{\mu_2}{\hbar} + \pi nf\right) - v_{\mathrm{F}}\Delta\mathcal{G}_{1,n}^{(e)}\left(\frac{\mu_2}{\hbar} - \pi nf\right)\right)\right]. \tag{20}$$

Equations (19) and (20) form the central result of this paper: they relate the dependence of the experimental signals on the control parameters on channel 2 (the chemical potential μ_2, the ac voltage amplitude V and the phase ϕ) to the single-particle coherence of the source. Inverting these relations basically leads to reconstruction of the single-electron coherence in frequency space and therefore we call this procedure a *single-electron quantum tomography protocol*.

3.3. Quantum tomography: the proposed experimental procedure

The experimental procedure reads as follows. First, one measures the excess zero-frequency partition noise $\Delta S_{11}^{\text{exp}} = \mathcal{R}\mathcal{T}\Delta \mathcal{Q}_0[\omega = 0, \mu_2, V_{\text{ac}}(t)]$ by subtracting the zero-frequency partition noise when the source is turned off. Then the μ_2 dependence of $\Delta \mathcal{Q}_0$ is measured by varying the chemical potential of ohmic contact 2.

To reconstruct the $n = 0$ harmonic of the single-electron coherence, no ac drive is applied on ohmic contact 2. By numerical derivation of the μ_2 dependence of the experimental data $\Delta \mathcal{Q}_0$, $\Delta \mathcal{G}_{1,n=0}^{(e)}(\mu_2/\hbar)$ is computed following equation (19).

To reconstruct the $n \neq 0$ harmonics of the single-electron coherence, the ac drive $V_{\text{ac}}(t) = V\cos(2\pi nft + \phi)$ is applied on ohmic contact 2. For $eV \ll nhf$, the measurement of $\Delta \mathcal{Q}_0$ provides a direct determination of $\bar{\chi}_n$, as $\bar{\chi}_n(\mu_2, \phi) \approx \frac{\Delta \mathcal{Q}_0[\omega=0,\mu_2,V_{\text{ac}}(t)]}{(eV/nhf)}$. By proceeding again to the numerical derivation of experimental data $\Delta \mathcal{Q}_0$, one gets the μ_2 dependence of $\frac{\partial \bar{\chi}_n}{\partial \mu_2}(\mu_2, \phi)$. It is computed for the two values, $\phi = 0$ and $\phi = \pi/2$, of the phase of the ac drive, to provide information on the real and imaginary parts of $\Delta \mathcal{G}_{1,n}^{(e)}(\omega)$. Indeed, using equation (20), one can relate adjacent values of the single-electron coherence distance by $2\pi nf$:

$$\Delta \mathcal{G}_{1,n}^{(e)}\left(\frac{\mu_2}{\hbar}\right) = \frac{h}{e^2 v_{\text{F}}}\left(\frac{\partial \bar{\chi}_n}{\partial \mu_2}(\mu_2 - \pi nf, \phi = 0) + i\frac{\partial \bar{\chi}_n}{\partial \mu_2}(\mu_2 - \pi nf, \phi = \pi/2)\right)$$
$$+ \Delta \mathcal{G}_{1,n}^{(e)}\left(\frac{\mu_2}{\hbar} - 2\pi nf\right). \qquad (21)$$

As $\Delta \mathcal{G}_{1,n}^{(e)}(\mu_2 = \pm\infty) = 0$, $\Delta \mathcal{G}_{1,n}^{(e)}(\mu_2)$ can be measured step by step starting from a point $\mu_2 = \mu_0$ where $\Delta \mathcal{G}_{1,n}^{(e)}(\mu_2 = \mu_0)$ is known to vanish.

To limit the total reconstruction time, an optimization strategy must be devised to choose the measurement points (i.e. the values of μ_2) so that regions where the coherence is expected to vary most are covered with maximal resolution. Such an optimization procedure is most conveniently performed when one has an idea of the expected experimental signal for the source to be characterized. That is why, in the next section, we will consider the problem of predicting the expected experimental signals.

Before discussing signal predictions, let us consider temperature effects since, in practice, the incoming channel has a finite electronic temperature T_{el}. The corresponding formulae are given in appendix A and show that the single-electron coherence $\Delta \mathcal{G}_1^{(e)}$ can only be accessed with an energy resolution $k_{\text{B}}T_{\text{el}}$. This stresses the necessity of working at the lowest possible temperature reachable by the experimental setup.

4. Predictions for the single-electron source

To support the implementation of our single-electron quantum tomography protocol, we present predictions for the on-demand single-electron source demonstrated in [9]. In particular, we

have computed the single-electron coherence and the experimentally accessible quantities $\Delta \mathcal{Q}_0(\mu_2) = \Delta \mathcal{Q}_0[\omega = 0, \mu_2, V_{ac}(t) = 0]$ and $\bar{\chi}_n(\mu_2, \phi)$.

As suggested by previous studies on the average current [9] and on finite-frequency current noise [10, 51] of this source, in the experimentally relevant regime of operation, interaction effects within the dot can be neglected. The appropriate formalism to discuss free-electron scattering in the presence of a periodic drive is the Floquet theory [52], which has been applied to quantum pumps by Moskalets and Büttiker [53, 54] and also to various driven nanoconductors by Hänggi and coworkers [55]. More recently, the fluctuations in the charge transferred by a mesoscopic turnstile have been predicted from Floquet theory by Battista and Samuelsson [56].

4.1. The Floquet approach to the mesoscopic capacitor

Here, we present the Floquet approach to the single-electron coherence emitted by a driven single-channel quantum conductor. Details specific to the mesoscopic capacitor are given in appendix B.

The Floquet scattering amplitude for electrons propagating through a driven quantum conductor is simply obtained as

$$\mathcal{S}_{Fl}(t, t') = \exp\left(\frac{ie}{\hbar} \int_{t'}^{t} V_d(\tau) \, d\tau\right) \mathcal{S}_0(t - t'), \tag{22}$$

where $V_d(\tau)$ is the periodic ac driving voltage applied to the dot and $\mathcal{S}_0(t - t')$ is the scattering amplitude across the undriven conductor, expressed in real time (see appendix B). Knowing the Floquet scattering amplitude (22) leads to the real-time single-electron coherence emitted by the driven mesoscopic conductor:

$$\mathcal{G}_1^{(e)}(t, t') = \int \mathcal{S}_{Fl}(t, \tau_+) \, \mathcal{S}_{Fl}(t', \tau_-)^* \, \mathcal{G}_{\mu_1}^{(e)}(\tau_+, \tau_-) \, d\tau_+ \, d\tau_-, \tag{23}$$

where $\mathcal{G}_{\mu_1}^{(e)}$ denotes the coherence function for electrons at chemical potential μ_1. However, as discussed before, we are interested in computing the single-electron coherence in the frequency domain. Therefore, we introduce the Floquet scattering matrix $\mathcal{S}_{Fl,n}(\omega)$, which represents the amplitude for photo-assisted transitions between single-electron states. It relates the single-particle modes emitted from the reservoir $c_1^{(res)}(\omega)$ to the single-electron modes emitted by the single-electron source as shown in figure 4(a). When the source is located close enough to the QPC, one expects decoherence and relaxation effects between the single-electron source and the QPC of the setup of figure 3(a) to be very weak. Assuming that they can be neglected, the modes emitted by the source can be identified with the incoming modes $c_1^{(in)}(\omega)$ of (8). We then have

$$c_1^{(in)}(\omega) = \sum_{n=-\infty}^{+\infty} \mathcal{S}_{Fl,n}(\omega) \, c_1^{(res)}(\omega + 2\pi n f). \tag{24}$$

Then, the nth harmonic $\mathcal{G}_{1,n}^{(e)}(\omega)$ can then be expressed in a form suitable for numerical computations:

$$v_F \mathcal{G}_{1,n}^{(e)}(\omega) = \sum_{k=-\infty}^{+\infty} \mathcal{S}_{Fl,k}(\omega + \pi n f) \, \mathcal{S}_{Fl,n+k}^*(\omega - \pi n f) \, n_F(\omega + (n + 2k)\pi f), \tag{25}$$
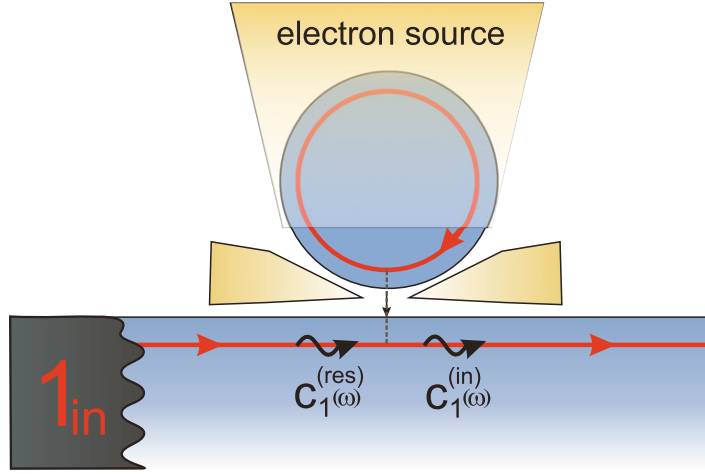
Figure 4. The incoming modes for the Floquet scattering formalism are the $c_1^{(res)}(\omega)$ issued by the reservoir (ohmic contact) and we assume that the outcoming modes from the source are directly injected into the QPC of figure 3(a) and thus are denoted by $c_1^{(in)}(\omega)$.

where $n_F(\omega)$ is the Fermi distribution at chemical potential μ_1 and temperature T_{el}. Taking the Fourier transform of (22), the Floquet scattering matrix $\mathcal{S}_{Fl,n}(\omega)$ can be computed in terms of the undriven conductor scattering matrix $\mathcal{S}_0(\omega)$ by

$$\mathcal{S}_{Fl,n}(\omega) = \sum_{k=-\infty}^{+\infty} C_k[V_d] C_{k+n}^*[V_d] \mathcal{S}_0(\omega - 2\pi k f), \tag{26}$$

where the coefficients $C_k[V_d]$ denote the Fourier transform of the phase accumulated by an electron experiencing the driving voltage $V_d(t)$ within the conductor:

$$\exp\left(\frac{ie}{\hbar} \int_{-\infty}^{t} V_d(\tau) d\tau\right) = \sum_{n=-\infty}^{+\infty} C_n[V_d] e^{-2\pi i n f t}. \tag{27}$$

4.2. Numerical results

Figure 5 shows $|v_F \Delta \mathcal{G}_{1,n}^{(e)}(\omega)|$ plots for realistic values of the parameters of the mesoscopic capacitor: the level spacing is $\Delta/k_B = 4.7$ K, the electronic temperature is $T_{el} \simeq 40$ mK and the driving frequency is $f = 3$ GHz. These results have been obtained by evaluating (25) numerically using a specific form for $\mathcal{S}_0(\omega)$ already used to interpret the experimental data [57], recalled in equation (B.1) and parameterized by the dot-to-lead transmission D. We have considered the case of a square voltage and a number of tests have been performed on the numerical results to ensure their validity (see appendix B).

When the dot is completely open ($D = 1$), $\Delta \mathcal{G}_1^{(e)}$ presents strong electron/hole coherences and, within the electron and hole quadrants, is localized close to the Fermi surface. The shape of the experimental signal $\Delta \mathcal{Q}_0(\mu_2)/e^2 f$ depicted in figure 6(a) can then be simply understood: an instantly responding system would lead to a triangular $\Delta \mathcal{Q}_0(\mu_2)$. This is a direct consequence
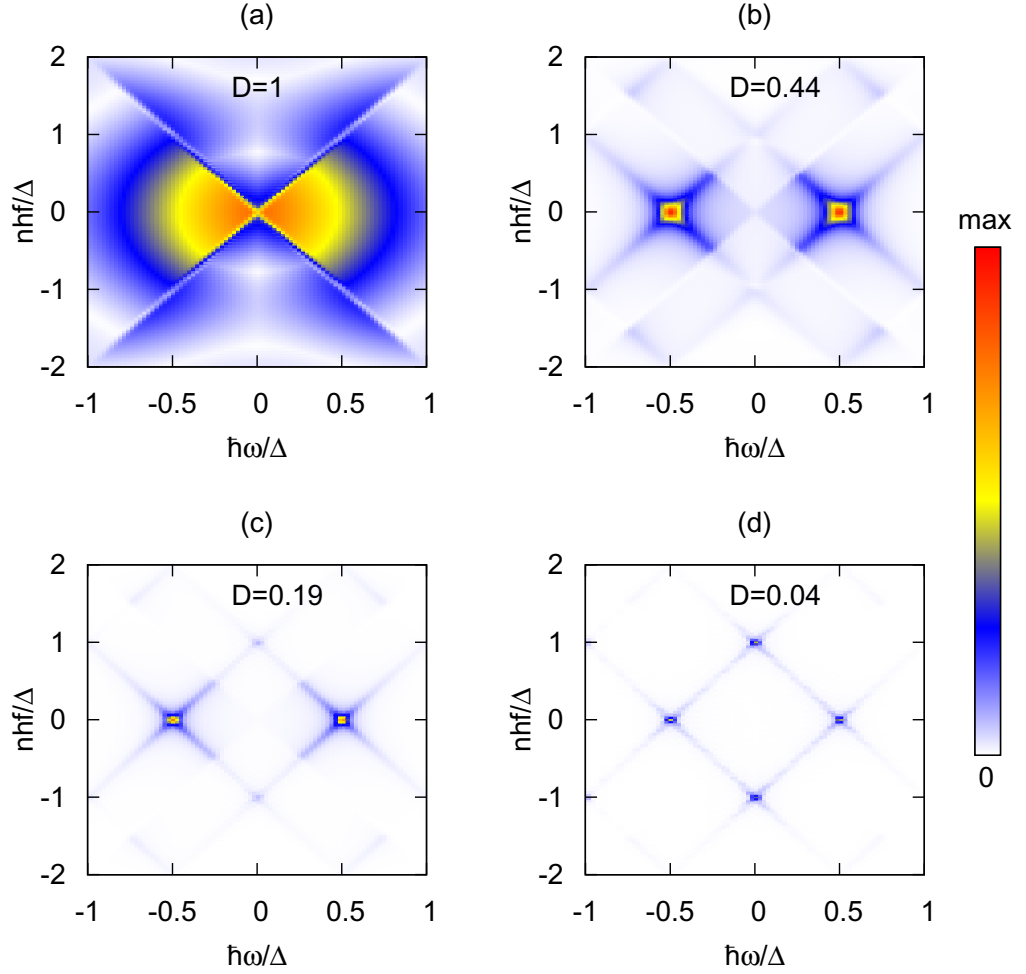
Figure 5. Density plot visualization of $|v_F \Delta \mathcal{G}_{1,n}^{(e)}(\omega)|$ at $f = 3\,\mathrm{GHz}$, $T_{\mathrm{el}} \simeq 40\,\mathrm{mK}$ and $\Delta / k_{\mathrm{B}} = 4.7\,\mathrm{K}$ for dot-to-lead transmission (a) $D = 1$, (b) $D = 0.44$, (c) $D = 0.19$ and (d) $D = 0.04$.

of the relation (19) between the electron distribution function and $\Delta \mathcal{Q}_0(\mu_2)$: in this situation, the square voltage would shift a fraction of electrons of energies between $-\Delta/2$ and 0 by Δ, thus sending them above the Fermi surface and giving rise to a triple step electron distribution function. The smoothed shape of the scattering theory prediction is due to the finite temperature and to the finite frequency response of the edge channel at frequencies comparable to h/Δ, the inverse of the time-of-flight around the dot.

When D decreases towards 0.19, $\Delta \mathcal{G}_{1,n}^{(e)}(\omega)$ concentrates around the $n = 0$, $\omega \simeq \pm \Delta/2\hbar$ points and simultaneously electron/hole coherences decrease, thus revealing energy-resolved single-electron and single-hole excitations. As we shall see in the next section, this is where the mesoscopic capacitor behaves as a good single-electron source.

Pinching the dot even more ($D = 0.04$) leads to the reappearance of electron/hole coherences (see figure 5(d)). In this regime, the source is driven too rapidly for single-electron and single-hole excitations to fully escape the cavity in a half-period ($\gamma_e T \simeq 2.15$) [9]. In fact,
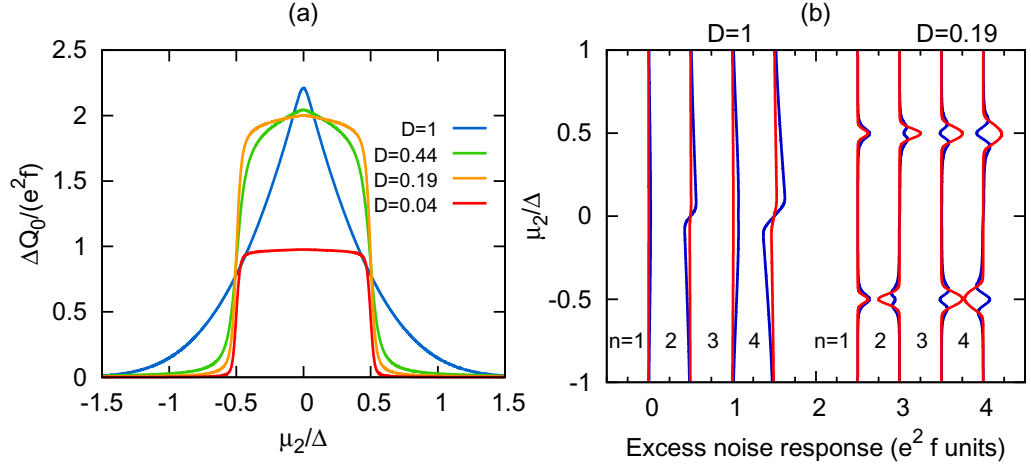
Figure 6. For the same values of D as in figure 5: (a) the expected $\Delta\mathcal{Q}_0(\omega = 0, \mu_2)$ as a function of μ_2/Δ and in units of $e^2 f \simeq 7.70 \times 10^{-29} \, \text{A}^2 \, \text{Hz}^{-1}$; (b) the expected $\bar{\chi}_n(\mu_2, \phi)$ for $n = 1$–4 with $\phi = 0$ (blue curves) and $\phi = \pi/2$ (red curves) as a function of μ_2/Δ and in units of $e^2 f$ for dot-to-lead transmission $D = 1$ and $D = 0.19$.

because at the end of each half-period, the electron or hole excitations to be emitted are still delocalized between the dot and the edge channel, the source produces a linear combination of the many-body states $|F_\mu\rangle$ and $\psi[\varphi_h]\psi^\dagger[\varphi_e]|F_\mu\rangle$ instead of a single-electron/hole pair state $\psi[\varphi_h]\psi^\dagger[\varphi_e]|F_\mu\rangle$. This is reflected by non-vanishing electron/hole coherences proportional to $\tilde{\varphi}_e(\omega_+)\,\tilde{\varphi}_h(\omega_-)^*$ corresponding to the spots in the (e/h) quadrants of figure 5(d).

Finally, in terms of current noise, let us stress that the amplitude of the experimental signals depicted in figure 6 is of the order of $10^{-29} \, \text{A}^2 \, \text{Hz}^{-1}$, above the resolution of standard noise measurements. A resolution of a few $10^{-30} \, \text{A}^2 \, \text{Hz}^{-1}$ has already been obtained [10, 32] in high-frequency noise measurements using the electron emitter presented in this paper. Noise floors below $10^{-30} \, \text{A}^2 \, \text{Hz}^{-1}$ were even reported in low-frequency noise measurements of electron pumps [58].

4.3. Quality of the single-electron source

Measurements of single-electron coherence of the source would lead to an assessment of its quality complementary to electron counting statistics [59]. Firstly, statistical properties of the source are described by the average number of electron excitations emitted per cycle and its fluctuation defined as the average value and fluctuation of the number of positive energy excitations:

$$N_+ = \int_0^{+\infty} c^\dagger(\omega)c(\omega)\,\mathrm{d}\omega, \tag{28}$$

where $c(\omega)$ and $c^\dagger(\omega)$ denote electron creation and destruction operators along the edge channel fed by the source. The average value $\langle N_+\rangle$ is clearly given as an integral of the diagonal part of the single-electron coherence of the source in the frequency domain. For the case of a periodic source of period T considered here, the average number $\bar{n}_+$ of electron excitations emitted per
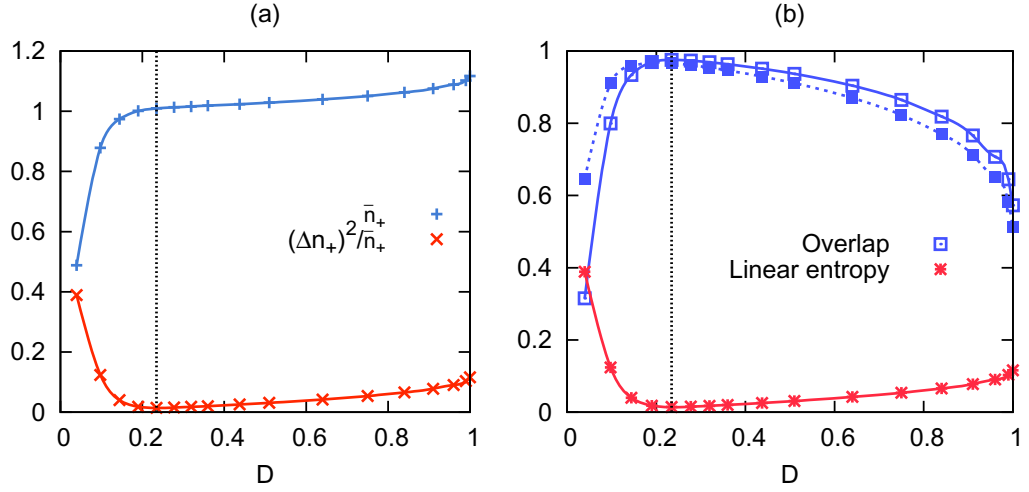
Figure 7. (a) Average number of electron excitations per cycle and its fluctuation as functions of D. (b) Linear entropy of electron excitations per emitted particle and overlap of single-electron coherence with the Lorentzian wavefunction as functions of D. The dashed curve gives the overlap per particle emitted. The optimal operating point corresponds to the vertical dotted line. All curves are obtained for $f = 3\,\mathrm{GHz}$, $T_{\mathrm{el}} \simeq 40\,\mathrm{mK}$ and $\Delta/k_{\mathrm{B}} = 4.7\,\mathrm{K}$.

period is then given by

$$\bar{n}_+ = T \int_0^{+\infty} v_{\mathrm{F}} \Delta \mathcal{G}_{n=0}^{(e)}(\omega)\, \frac{\mathrm{d}\omega}{2\pi}. \tag{29}$$

Generically, the fluctuation $\langle N_+^2 \rangle - \langle N_+ \rangle^2$ involves a second-order electronic coherence but assuming that the source is described within Floquet scattering theory, Wick's theorem enables us to express the fluctuation of N_+ in terms of the single-particle coherence. For a periodic source, the fluctuation Δn_+ of the number of electron excitations produced per period is then given as an integral of single-electron coherence over the (e/h) quadrants, thus stressing the role of coherent electron/hole pairs in fluctuations:

$$(\Delta n_+)^2 = T \sum_{n=1}^{+\infty} \int_{-\pi nf}^{\pi nf} \left| v_{\mathrm{F}} \Delta \mathcal{G}_n^{(e)}(\omega) \right|^2 \frac{\mathrm{d}\omega}{2\pi}. \tag{30}$$

Scattering theory predictions for these quantities are depicted in figure 7(a) as functions of the dot transparency. When $D \to 1$, the electron number is not quantized: $\bar{n}_+$ is slightly greater than one and fluctuations are of the order of 0.3. In the shot noise regime where $D \ll 1$, the electron does not have the time to leave the quantum dot in time $T/2$ and this translates into a decay of $\bar{n}_+$ and an increase of relative fluctuations $(\Delta n_+)^2/\bar{n}_+ \to 1/2$ consistent with predictions from the probabilistic model of [59]. In the intermediate region, quantization of the emitted number of electron excitations per period is observed: at $D \simeq 0.22$, we find that $\bar{n}_+ \simeq 1.009$ and $(\Delta n_+)^2/\bar{n}_+ \simeq 0.014$ ($\Delta n_+ \simeq 0.12$).

This is the quantum jitter regime where the current noise reflects the randomness of electron emission through quantum tunneling [10]. In this regime, almost certainly one electron and one hole are emitted during each period [59]. From a statistical point of view, the optimal point for

single-electron emission is when $\bar{n}_+ \simeq 1$ and Δn_+ is minimal which occurs for $D \simeq 0.22$ with our choice of parameters.

Next, to assess the source's quantum coherence, we propose to use the linear entropy of the reduced density operator for electron excitations as well as its overlap of $\Delta \mathcal{G}_1^{(e)}$ with the Lorentzian wavefunction expected in a discrete level model. The linear entropy measures how far the reduced density operator for electron excitations departs from a pure state [60]. The overlap with a given electron wavefunction gives the probability that, per cycle, an electron is detected in this single-particle state. For a periodic source, the linear entropy production per emitted electron is given by

$$S_{\mathrm{L}} = 1 - \frac{T}{\bar{n}_+} \sum_{n=-\infty}^{+\infty} \int_{|n|\pi f}^{+\infty} |v_{\mathrm{F}} \Delta \mathcal{G}_n^{(e)}(\omega)|^2 \, \frac{\mathrm{d}\omega}{2\pi}. \tag{31}$$

In the same way, the fidelity with respect to a normalized electron wavefunction φ_{e} expressed in the frequency domain as $\tilde{\varphi}_{\mathrm{e}}(\omega) = \int \varphi_{\mathrm{e}}(x) \mathrm{e}^{\mathrm{i}\omega x/v_{\mathrm{F}}} \, \mathrm{d}x$ can be computed in terms of the single-electron coherence:

$$\mathcal{F}(\mathcal{G}^{(e)}|\varphi_{\mathrm{e}}) = \sum_{n=-\infty}^{+\infty} \int_{|n|\Omega_T}^{+\infty} \Delta \mathcal{G}_n^{(e)}(\omega) \, \tilde{\varphi}_{\mathrm{e}}^*(\omega + n\pi f) \tilde{\varphi}_{\mathrm{e}}(\omega - n\pi f) \, \frac{\mathrm{d}\omega}{2\pi}. \tag{32}$$

In the case of the single-electron source, it is natural to choose as a trial wavefunction $\tilde{\varphi}_{\mathrm{e}}(\omega)$ a truncated Lorentzian wavefunction (7) representing the result of the decay from a resonant level at energy $\hbar\omega_{\mathrm{e}} = \Delta/2$ into the semi-infinite continuum of accessible electron states.

Predictions for the linear entropy (31) and for the overlap (32) with this resonant level wavefunction are depicted in figure 7(b) for experimentally reasonable parameters. In this case, we see that the best operating point is obtained for $D \simeq 0.22$. At this optimal point, the source is predicted to be highly coherent and well described by the discrete level model wavefunctions. In particular, the fidelity per emitted electron between the reduced density operator for electron-like excitations and the resonant level wavefunction is 0.97 and the purity is 0.99. As stated before, decreasing D does not leave enough time for emitting single-electron and single-hole excitations. This leads to the generation of electron/hole coherence responsible for quantum fluctuations of N_+ and also for the lower purity of single-electron and single-hole excitations.

5. Conclusion

To conclude, we have proposed a quantum tomography protocol to reconstruct the quantum state of single-electron excitations in quantum Hall edge channels. Its implementation would provide a complete assessment of the quantum coherence of single-electron sources, either energy resolved [9, 11, 56] or time resolved [31]. In particular, by probing harmonics $\Delta \mathcal{G}_n^{(e)}$ up to $nf = 10$ GHz or more, it would give access to the individual electronic wavepackets on a sub-nanosecond time scale.

This experimental breakthrough could then be used for quantitative studies of decoherence and relaxation of single-electron excitations [28] complementary to recent studies of non-equilibrium electronic relaxation in quantum Hall edge channels [27, 61]. A new generation of experiments aiming at the controlled manipulation of the quantum state of a single to a few electrons could then be envisioned in the near future. In particular, new experiments could involve decoherence engineering as in [62], where a voltage probe increases decoherence at will

IOP Institute of Physics Φ DEUTSCHE PHYSIKALISCHE GESELLSCHAFT

within a Mach–Zehnder interferometer. An important issue is quantum coherence protection as in [63], where electronic decoherence is limited through an appropriate sample design. Another exciting albeit challenging perspective is to combine electron coherence measurements, photon statistics measurement [64] and single-electron sources in order to explore the non-classicality of photons radiated by an electric current carried by trains of coherent electrons [65].

Acknowledgments

Appendix A. Finite-temperature effects on single-electron tomography

Let us consider the case of a source at finite electronic temperature T_{el} on channel 2. Then, equation (19) becomes

$$\left(\frac{\partial \Delta \mathcal{Q}_0}{\partial \mu_2}\right)(\mu_2, T_{el}) = -\frac{2e^2}{h} \int_{-\infty}^{+\infty} \frac{v_F \Delta \mathcal{G}_{1,n=0}^{(e)}\left(\frac{\mu_2}{\hbar} + \frac{k_B T_{el}}{\hbar} x\right)}{4 \cosh^2(x/2)} \, dx, \tag{A.1}$$

whereas equation (20) has to be replaced by

$$\left(\frac{\partial \bar{\chi}_n}{\partial \mu_2}\right)(\mu_2, T_{el}) = \frac{e^2}{h} \int_{-\infty}^{+\infty} \frac{G(n, \phi, \mu_2 + k_B T_{el} x)}{4 \cosh^2(x/2)} \, dx, \tag{A.2}$$

where

$$G(n, \phi, \mu) = \Re\left[e^{i\phi}\left(v_F \mathcal{G}_{1,n}^{(e)}\left(\frac{\mu}{\hbar} + \pi n f\right) - v_F \mathcal{G}_{1,n}^{(e)}\left(\frac{\mu}{\hbar} - \pi n f\right)\right)\right]. \tag{A.3}$$

As is clear for these expressions, the single tomography protocol would then reconstruct a convolution of the single-electron coherence in channel 1 with a thermal smearing function of width $k_B T_{el}$.

Appendix B. The driven mesoscopic capacitor

The mesoscopic capacitor is modeled as in [57] as an electronic Fabry–Perot cavity whose transparency is modulated by the transmission D of its QPC. Here Δ denotes the level spacing within the quantum dot (electronic cavity). The scattering matrix for the undriven mesoscopic capacitor is given by [57]

$$\mathcal{S}_0(\varepsilon) = \frac{\sqrt{1-D} - e^{2\pi i \varepsilon/\Delta}}{1 - \sqrt{1-D}\, e^{2\pi i \varepsilon/\Delta}}. \tag{B.1}$$

This choice assumes that in the absence of drive, the Fermi level of channel 1 is equidistant from two consecutive energy levels of the dot, a situation that can always be realized by applying an appropriate dc voltage. Here, the electron escape time from the dot is given by $\gamma_e = (\Delta/h) \times 2D/(2-D)$ [10].

In principle, our formalism can be applied for any drive voltage. In particular, we could implement the precise form generated by the voltage generator used in the experiment taking

into account its limitations. But in this paper, we have considered that a T periodic square drive voltage is applied to the mesoscopic capacitor: $V(t) = V_d$ for $0 \leqslant t < T/2$ and $V(t) = -V_d$ for $-T/2 \leqslant t < 0$ and we have chosen its amplitude $2eV_d$ to be equal to the level spacing Δ. In this case, the Fourier coefficients of the driving phase are then given by

$$C_n[V] = \frac{2}{\pi} \sin\left(\frac{\pi}{2}(\mathcal{A} - n)\right) \frac{\mathcal{A}}{\mathcal{A}^2 - n^2} e^{i(n\pi/2 - \mathcal{A})}, \quad \text{for } n \neq \mathcal{A}, \tag{B.2}$$

$$= 1/2 \quad \text{otherwise}, \tag{B.3}$$

with $\mathcal{A} = eV_d/2hf$.

The images produced for this paper represent $|\Delta\mathcal{G}_n^{(e)}(\omega)|$ for $|n| \leqslant 100$ and $|\hbar\omega| \leqslant 2\Delta$. Numerical convergence was achieved by summing over 4000 harmonics. Various tests have been performed such as hermiticity $\mathcal{G}_n^{(e)}(\omega)^* = \mathcal{G}_{-n}^{(e)}(\omega)$ and electron/hole symmetry $\Delta\mathcal{G}_n^{(e)}(-\omega) = (-1)^{n+1}\Delta\mathcal{G}_n^{(e)}(\omega)$. The total charge emitted per cycle has been computed and neutrality has been checked up to 10^{-5}. Finally, the Cauchy–Schwarz inequality satisfied by $\mathcal{G}^{(e)}$ has also been checked numerically as well as the behavior with respect to time translation of the driving signal.

References

[1] Deléglise S, Dotsenko I, Sayrin C, Bernu J, Brune M, Raimond J M and Haroche S 2008 *Nature* **455** 510
[2] Hofheinz M *et al* 2009 *Nature* **459** 546
[3] Ourjmoumtsev A, Jeong H, Tualle-Brouri R and Grangier P 2007 *Nature* **448** 784
[4] Ji Y, Chung Y, Sprinzak D, Heiblum M, Mahalu D and Shtrikman H 2003 *Nature* **422** 415
[5] Roulleau P, Portier F, Glattli D C, Roche P, Cavanna A, Faini G, Gennser U and Mailly D 2008 *Phys. Rev. Lett.* **100** 126802
[6] Neder I, Marquardt F, Heiblum M, Mahalu D and Umansky V 2007 *Nat. Phys.* **3** 534
[7] Neder I, Ofek N, Chung Y, Heiblum M, Mahalu D and Umansky V 2007 *Nature* **448** 333
[8] Samuelsson P, Sukhorukov E and Büttiker M 2004 *Phys. Rev. Lett.* **92** 026805
[9] Fève G, Mahé A, Berroir J, Kontos T, Plaçais B, Glattli D C, Cavanna A, Etienne B and Jin Y 2007 *Science* **316** 1169
[10] Mahé A, Parmentier F D, Bocquillon E, Berroir J, Glattli D C, Kontos T, Plaçais B, Fève G, Cavanna A and Jin Y 2010 *Phys. Rev.* B **82** 201309
[11] Leicht C, Mirowski P, Kaestner B, Hols F, Kashcheyevs V, Kurganova E V, Zeitler U, Weimann T, Pierz K and Schumacher H W 2011 *Semicond. Sci. Technol.* **26** 055010
[12] Blumenthal M D, Kaestner B, Li L, Giblin S, Janssen T J B M, Pepper M, Anderson D, Jones G and Ritchie D A 2007 *Nat. Phys.* **3** 343
[13] Talyanskii V I, Shilton J M, Pepper M, Smith C G, Ford C J B, Linfield E H, Ritchie D A and Jones G A C 1997 *Phys. Rev.* B **56** 15180
[14] Ahlers F-J, Kieler O F O, Sagol B E, Pierz K and Siegner U 2006 *J. Appl. Phys.* **100** 093702
[15] Hermelin S, Takada S, Yamamoto M, Tarucha S, Wieck A D, Saminadayar L, Baüerle C and Meunier T 2011 arXiv:1107.4759
[16] Ol'khovskaya S, Splettstoesser J, Moskalets M and Büttiker M 2008 *Phys. Rev. Lett.* **101** 166802
[17] Splettstoesser J, Moskalets M and Büttiker M 2009 *Phys. Rev. Lett.* **103** 076804
[18] Beenakker C 2006 *Quantum Computers Algorithms and Chaos* (*Int. School of Physics Enrico Fermi* vol 162) ed G Casati, D Shepelyansky, P Zoller and G Benenti (Amsterdam: IOS Press) pp 307–47
[19] Chung V W, Samuelsson P and Büttiker M 2005 *Phys. Rev.* B **72** 125320
[20] Chalker J, Gefen Y and Veillette M 2007 *Phys. Rev.* B **76** 085320
[21] Neder I and Marquardt F 2007 *New J. Phys.* **9** 112

[22] Neuenhahn C and Marquardt F 2008 *New J. Phys.* **10** 115018
[23] Levkivskyi I and Sukhorukov E 2008 *Phys. Rev.* B **78** 045322
[24] Roulleau P, Portier F, Roche P, Cavanna A, Faini G, Gennser U and Mailly D 2008 *Phys. Rev. Lett.* **101** 186803
[25] Kovrizhin D L and Chalker J T 2009 *Phys. Rev.* B **80** 161306
[26] Altimiras C, Le Sueur H, Gennser U, Cavanna A, Mailly D and Pierre F 2009 *Nat. Phys.* **6** 34
[27] Le Sueur H, Altimiras C, Gennser U, Cavanna A, Mailly D and Pierre F 2010 *Phys. Rev. Lett.* **105** 056803
[28] Degiovanni P, Grenier C and Fève G 2009 *Phys. Rev.* B **80** 241307
[29] Smithey D T, Beck M, Raymer M G and Faridani A 1993 *Phys. Rev. Lett.* **70** 1244
[30] Lvovsky A I and Raymer M G 2009 *Rev. Mod. Phys.* **81** 299–332
[31] Keeling J, Klich I and Levitov L 2006 *Phys. Rev. Lett.* **97** 116403
[32] Parmentier F D, Mahé A, Denis A, Berroir J M, Glattli D C, Plaçais B and Fève G 2011 *Rev. Sci. Instrum.* **82** 013904
[33] Glauber R 1963 *Phys. Rev.* **130** 2529
[34] Keeling J, Shytov A and Levitov L 2008 *Phys. Rev. Lett.* **101** 196404
[35] Abrikosov A, Gorkov L and Dzyaloshinski I 1963 *Methods of Quantum Field Theory in Statistical Physics* (New York: Dover)
[36] Mahé A, Parmentier F D, Fève G, Berroir J M, Kontos T, Cavanna A, Etienne B, Jin Y, Glattli D C and Plaçais B 2008 *J. Low Temp. Phys.* **153** 339
[37] Samuelsson P and Büttiker M 2006 *Phys. Rev.* B **73** 041305
[38] Hanbury Brown R and Twiss R 1956 *Nature* **177** 27
[39] Liu R, Odom B, Yamamoto Y and Tarucha S 1998 *Nature* **391** 263
[40] Henny M, Oberholzer S, Strunk C, Heinzel T, Ensslin K, Holland M and Schönenberger C 1999 *Science* **284** 296
[41] Oliver W, Kim J, Liu R and Yamamoto Y 1999 *Science* **284** 299
[42] Hong C, Ou Z and Mandel L 1987 *Phys. Rev. Lett.* **59** 2044
[43] Hanbury Brown R and Twiss R 1956 *Nature* **178** 1046
[44] Reznikov M, Heiblum M, Shtrikman H and Mahalu D 1995 *Phys. Rev. Lett.* **75** 3340–3
[45] Kumar A, Saminadayar L, Glattli D C, Jin Y and Etienne B 1996 *Phys. Rev. Lett.* **76** 2778
[46] Lesovik G and Levitov L 1994 *Phys. Rev. Lett.* **72** 538
[47] Pedersen M H and Büttiker M 1998 *Phys. Rev.* B **58** 12993–3006
[48] Blanter Y and Buttiker M 2000 *Phys. Rep.* **336** 1
[49] Schoelkopf R J, Kozhevnikov A A, Prober D E and Rooks M J 1998 *Phys. Rev. Lett.* **80** 2437–40
[50] Reydellet L H, Roche P, Glattli D C, Etienne B and Jin Y 2003 *Phys. Rev. Lett.* **90** 176803
[51] Moskalets M, Samuelsson P and Büttiker M 2008 *Phys. Rev. Lett.* **100** 086601
[52] Floquet G 1883 *Ann. Ecole Norm. Sup.* **12** 47
[53] Moskalets M and Büttiker M 2002 *Phys. Rev.* B **66** 205320
[54] Moskalets M and Büttiker M 2007 *Phys. Rev.* B **75** 035315
[55] Kohler S, Lehmann J and Hänggi P 2005 *Phys. Rep.* **406** 379–443
[56] Battista F and Samuelsson P 2011 *Phys. Rev.* B **83** 125324
[57] Gabelli J, Fève G, Berroir J, Plaçais B, Cavanna A, Etienne B, Jin Y and Glattli D C 2006 *Science* **313** 499
[58] Maire N, Hohls F, Kaestner B, Pierz K, Schumacher H and Haug R 2008 *Appl. Phys. Lett.* **92** 082112
[59] Albert M, Flindt C and Büttiker M 2010 *Phys. Rev.* B **82** 041407
[60] Nielsen M and Chuang I 2000 *Quantum Computation and Quantum Information* (Cambridge: Cambridge University Press)
[61] Degiovanni P, Grenier C, Fève G, Altimiras C, le Sueur H and Pierre F 2010 *Phys. Rev.* B **81** 121302
[62] Roulleau P, Portier F, Roche P, Cavanna A, Faini G, Gennser U and Mailly D 2009 *Phys. Rev. Lett.* **102** 236802
[63] Altimiras C, Le Sueur H, Gennser U, Cavanna A, Mailly D and Pierre F 2010 *Phys. Rev. Lett.* **105** 226804
[64] Zakka-Bajjani E, Dufouleur J, Coulombel N, Roche P, Glattli D C and Portier F 2010 *Phys. Rev. Lett.* **104** 206802
[65] Beenakker C and Schomerus H 2004 *Phys. Rev. Lett.* **93** 096801